Catalysis Science & Technology

Selective catalytic reduction of NO over Cu-AFX zeolites: Mechanistic insights from in situ/operando spectroscopic and DFT studies

Journal:	*Catalysis Science & Technology*
Manuscript ID	CY-ART-02-2021-000282.R1
Article Type:	Paper
Date Submitted by the Author:	24-Apr-2021
Complete List of Authors:	Liu, Chong; Chinese Academy of Sciences Fujian Institute of Research on the Structure of Matter, Institute for Catalysis; Kubota, Hiroe; Hokkaido University, Institute for Catalysis Amada, Takehiro; Hokkaido University, Institute for Catalysis Toyao, Takashi; Hokkaido university, Institute for Catalysis Maeno, Zen; Hokkaido University, Institute for Catalysis Ogura, Masaru; Institute of Industrial Science, The University of Tokyo, Department of Materials and Environmental Science Nakazawa, Naoto; Yokohama National University Inagaki, Satoshi; Yokohama National University, a. Division of Materials Science and Chemical Engineering Kubota, Yoshihiro; Yokohama National University Shimizu, Ken-ichi; Hokkaido University

Selective catalytic reduction of NO over Cu-AFX zeolites: Mechanistic insights from *in situ*/*operando* spectroscopic and DFT studies

Chong Liu,*[,§] Hiroe Kubota,[†] Takehiro Amada,[†] Takashi Toyao,[†,‡] Zen Maeno,[†] Masaru Ogura,[#] Naoto Nakazawa,[∥] Satoshi Inagaki,[∥] Yoshihiro Kubota,[∥] Ken-ichi Shimizu*[,†,‡]

[§] State Key Laboratory of Structural Chemistry, Fujian Institute of Research on the Structure of Matter, Chinese Academy of Sciences, Fuzhou, Fujian 350002, China

[†] Institute for Catalysis, Hokkaido University, N-21, W-10, Sapporo 001-0021, Japan

[‡] Elements Strategy Initiative for Catalysts and Batteries, Kyoto University, Katsura, Kyoto 615-8520, Japan

[#] Institute of Industrial Science, The University of Tokyo, 4-6-1 Komaba, Meguro-ku, Tokyo 153-8505, Japan

[∥] Division of Materials Science and Chemical Engineering, Yokohama National University, 79-5 Tokiwadai, Hodogaya-ku, Yokohama 240-8501, Japan

Corresponding authors

*Ken-ichi Shimizu (kshimizu@cat.hokudai.ac.jp)

*Chong Liu (chongliu@fjirsm.ac.cn)

Abstract

In situ/operando spectroscopic experiments and DFT calculations were combined to study the selective catalytic reduction of NO with NH_3 (NH_3–SCR) over Cu-AFX zeolites. Transient experiments (*in situ/operando* XANES, IR, and UV-vis) on the reduction half cycle show that the NH_3 coordinated on the Cu(II) center reacts with NO to produce N_2 and H_2O, and simultaneously Cu(II) is reduced to Cu(I). On the other hand, transient experiments on the oxidation half cycle indicate that the oxidation of Cu(I) to Cu(II) species occurs with O_2 as the sole oxidant. DFT calculations suggest plausible pathways for the oxidative activation of Cu(I) by O_2 as the only oxidant. It is proposed that the oxidation of Cu(I) by exclusive O_2 rather than the NO-assisted oxidation plays the key role in the standard NH_3–SCR reaction at low temperatures.

Keywords: NH_3–SCR, Cu-AFX, *In situ/operando* spectroscopy, XAS, DFT calculation

1. Introduction

Selective catalytic reduction of nitrogen oxides (NO_x) using NH_3 as the reducing agent (NH_3–SCR) is utilized to control the pollutant emissions from diesel engines.[1–3] Among various catalysts studied,[4–9] Cu-exchanged small-pore zeolites, such as Cu-CHA, are among the most promising catalysts due to their hydrothermal durability.[10–17] The three-dimensional pore system of CHA is formed by stacking of double-6-ring (d6r) in an AABBCC packing sequence.[18,19] Access into the large chabazite cages (diameter: ~0.73 nm) is limited by 8-ring (8R) windows (diameter: ~0.38 nm), which allows stabilization of isolated copper cations under NH_3–SCR and hydrothermal conditions.[10]

Toward rational design of NH_3–SCR catalysts, significant efforts have been focused on the molecular level understanding of the NH_3–SCR on Cu-zeolites.[20] It is widely accepted that isolated Cu cations coordinated with NH_3 play a key role in the NH_3–SCR,[21,22] and the catalytic reaction is driven by the Cu(II)↔Cu(I) redox cycle.[22–29] The reduction half reaction has been well understood. Based on the *in situ* spectroscopic measurements over Cu-CHA catalysts,[22,30,31] the Cu(II) → Cu(I) reduction is described as Eqn (1).

$$[Cu(NH_3)_3(OH)]^+ + NO \rightarrow [Cu(NH_3)_2]^+ + N_2 + 2H_2O \quad (1)$$

In contrast, rather few *in situ* spectroscopic observations of the oxidation half cycle have been reported, for which the detailed mechanisms remain in debate. Computational studies show that dissociation of O_2 over a single $[Cu(NH_3)_2]^+$ complex requires high activation barrier, which is unlikely to occur.[32,33] Gao et al.[24] and Paolucci et al.[25] have suggested the oxidation of Cu(I) species proceeds via Cu dimer species. The $[Cu(NH_3)_2]^+$ complexes in Cu-CHA show high mobility due to the weak interaction with the zeolite framework,[25] and two mobile $[Cu(NH_3)_2]^+$ react with one O_2 molecule to produce a dimeric copper complex, i.e. $[Cu_2O_2(NH_3)_4]^{2+}$ [(Eqn. (2)].[2425] The production of isolated mononuclear Cu(II) from the activated $[Cu_2O_2(NH_3)_4]$ was suggested to occur via NO assistance [Eqn. (3)].

$$2[Cu(NH_3)_2]^+ + O_2 \rightarrow [Cu_2O_2(NH_3)_4]^{2+} \quad (2)$$

$$[Cu_2O_2(NH_3)_4]^{2+} + 2NO + 4NH_3 \rightarrow 2[Cu(NH_3)_3(OH)]^+ + 2N_2 + 2H_2O \quad (3)$$

Very recently, several groups[3435] reported spectroscopic evidences for the structure of $[Cu_2O_2(NH_3)_4]^{2+}$, both pointing that a side-on (μ-η^2,η^2-peroxo) dicopper (II) complex rather than bis(μ-oxo) dicopper(III) is mainly produced after the reaction of two $[Cu(NH_3)_2]^+$ with O_2. Although most early DFT data[25,32,36] predicted a higher stability of the latter structure, it has been shown the stability of these dicopper complexes depends on the chosen functionals.[37]

Our group[31,36] reported experimental and theoretical studies on the redox mechanism of NH_3–SCR over Cu-CHA and proposed the catalytic pathway consisting of reactions (1), (2), and (4).

$$4[Cu(NH_3)_2]^+ + O_2 + 4NH_3 + 2H_2O \rightarrow 4[Cu(NH_3)_3(OH)]^+ \quad (4)$$

Eqn. (4) describes the oxidation half reaction proceeds with O_2 as the sole oxidant, which is a non-NO-assisted process in contrast to Eqn. (3). The sum of the reactions (1) and (4) affords the stoichiometry of the standard NH_3–SCR [Eqn. (5)].

$$4NO + 4NH_3 + O_2 \rightarrow 4N_2 + 6H_2O \quad (5)$$

As an alternative to CHA, AFX is another 8R small-pore zeolite, which consists of *aft* cage (0.55 × 1.35 nm) and small *gme* cage (0.33 × 0.74 nm). Kubota et al.[38] recently developed a AFX zeolite using a bulky and non-flexible organic structure-directing agent (OSDA), and the obtained AFX shows a higher stability than the conventional AFX-type zeolite (SSZ-16) as a consequence of being synthesized with a flexible OSDA.[39] The Cu-exchanged AFX (Cu-AFX) has been shown to exhibit high catalytic performance for NH_3–SCR.[40–42]

In this study, we investigate the standard NH_3–SCR over Cu-AFX zeolites using *in situ*/*operando* X-ray absorption near-edge structure (XANES), IR, and UV-vis techniques in combination with DFT calculations. We show the results of spectroscopic measurements under steady-state and transient NH_3–SCR conditions. Together with the DFT study on oxidation half cycle, the overall mechanism of NH_3–SCR over Cu-AFX zeolite is discussed.

2. Materials and methods

2.1 Preparation of the catalysts

NH_4^+-form of AFX (Si/Al = 5.3), prepared according to the procedures by Kubota et al.,[38] was supplied from the Research Association of Automotive Internal Combustion Engines (AICE), Japan. H^+-exchanged AFX was prepared by calcining NH_4^+-AFX at 600 °C for 1 h under air. Cu-AFX was prepared by ion-exchange method using $Cu(NO_3)_2$ solution at a pH 5.5, followed by washing with distilled water three times, drying at 100 °C for 24 h, and then the sample was calcinated under air at 600 °C for 1 h. The Cu loading amounts were determined by the energy-dispersive X-ray fluorescence spectrometry (EDX-700HS, Shimadzu Corp.). Three zeolite catalysts with varying Cu/Al ratios of 0.02, 0.13, and 0.25 (Cu loading = 0.4, 2.1, and 4.1 wt%) were used (Table 1), which were denoted as Cu*x*-AFX (*x* is the Cu loading in wt %).

Table1. Structural properties the Cu*x*-AFX zeolite catalysts.[a]

Zeolite sample	Si/Al	Cu loading (wt%)	Cu/Al	Cu density (Cu/1000Å^3)	Mean Cu–Cu distance (Å)
Cu0.4-AFX	5.3	0.4	0.02	0.06	32.4
Cu2.1-AFX	5.3	2.1	0.13	0.30	18.5
Cu4.1-AFX	5.3	4.1	0.25	0.60	14.7

[a]*x* denotes the Cu loading in wt%. The Cu density/mean Cu–Cu distance were determined with the assumption that the Cu species are homogenously distributed in AFX zeolite (details in supplementary information).

2.2 *In situ/operando* spectroscopic experiments

Cu K-edge XAS measurements were carried out in transmission mode at beamline BL14B2 in SPring-8 (Harima, Japan). Linear combination fitting (LCF) analysis of XANES spectra were performed with the Athena software.[43] The reference compounds include the solution-phase complexes of $[Cu(NH_3)_2]^+$ and $[Cu(NH_3)_4]^{2+}$ prepared according to the literature[23,44] as well as the *in situ* generated Z-$[Cu^{2+}]$ (Z = zeolite framework). Diffuse reflectance UV-vis experiments were conducted using a UV-vis spectrometer (JASCO V-670) with an *in situ* flow cell. IR spectra were measured in a transmission mode using JASCO FT/IR-4600, which was equipped with a quartz cell connected to a conventional flow reaction system. The relative concentrations of N_2 in the outlet gas mixture during UV-vis and IR experiments were monitored by the mass spectroscopy apparatus (BELMass, MicrotracBEL Corp.). Detailed descriptions of the *in situ/operando* XAS, IR, and UV-vis measurements[31] are provided in supplementary information. The XAS and UV-vis spectra under steady-state were taken after checking that spectra did not change as a function of time.

2.3 Computational details

Spin-polarized periodic DFT calculations were performed using the Vienna Ab initio Simulation Package (VASP).[45–47] The generalized gradient approximation (GGA) based on Perdew-Burke-Ernzerhof (PBE) exchange-correlation functional in combination with the projector augmented waves (PAW) method was used.[48–50] The kinetic cutoff energy of the plane-wave basis set was set to 500 eV. A Gaussian smearing of 0.05 eV was applied to band occupations around the Fermi level, and the total energies were extrapolated to $\sigma \rightarrow 0$. Brillouin zone sampling was restricted to the Γ point.[51] The dispersion-corrected DFT-D3(BJ) method was used to describe the van der Waals interactions.[52] Convergence was assumed when the force on each atom was below 0.05 eV $Å^{-1}$. The climbing image nudged elastic band (CI-NEB) method was used to determine the minimum-energy reaction paths and the corresponding transition states.[53] The maximum energy geometries along the reaction coordinates obtained with the CI-NEB method were further optimized using the quasi-Newton algorithm. The energetics of the reaction intermediates and transition states with their most stable spin states were used to construct the minimum-energy reaction paths. Chen et al.[37] compared different density functionals for O_2 activation over $[Cu(NH_3)_2]^+$ complexes in Cu-CHA and suggested a Hubbard-U correction is necessary for the reasonable accuracy of the simulated systems. Therefore, we also included the Hubbard term correction, and a U-parameter of 6 eV was used for the Cu 3d states.[37,54]

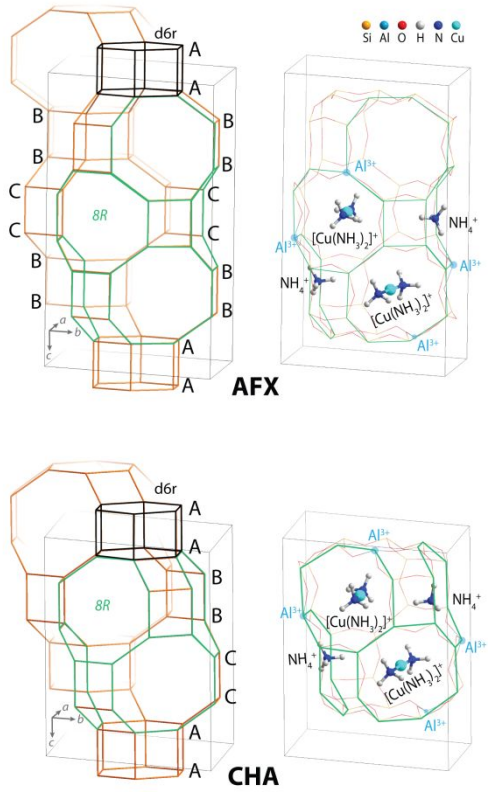

Fig. 1 AFX and CHA zeolite frameworks with three-dimensional eight-ring (8R) pore structures (left), and computational models of AFX and CHA unit cells with two $[Cu(NH_3)_2]^+$ and two Brønsted acid sites (in the form of NH_4^+) in zeolite cages (right).

The NH_3–SCR chemistry was investigated for Cu-AFX zeolite and compared with our previous report on Cu-CHA.[36] Both AFX and CHA frameworks possess three-dimensional structures with 8R pores, which have diameters of 3.4 × 3.6 Å and 3.8 × 3.8 Å, respectively (Fig. 1). The cavities of AFX and CHA are composed from the different stackings of double-six-ring (d6r) units along the [001] direction. The AFX framework contains two types of cages: the *gme* cage with a BBCC sequence and the *aft* cage with an AABBCCBB sequence. In comparison, the CHA framework has an AABBCC sequence of the six-rings, forming a so-called *cha* cage. For the DFT calculations, a hexagonal unit cell ($Si_{48}O_{96}$) was employed for the AFX zeolite (Fig. 1).[55] The initial computational model was constructed by introducing two $[Cu(NH_3)_2]^+$ complexes and two Brønsted acid sites (BASs) inside the *aft* cage of AFX zeolite. Under NH_3–SCR atmosphere, the Brønsted protons (H^+) were transferred to ammonia molecules, which form the ionic adsorption complexes (NH_4^+).[31,56] Therefore, the NH_4^+ sites rather than bare H^+ were used for the elementary reactions with the participation of BASs. Charge-compensation was provided by the substitution of Al^{3+} for framework Si^{4+}, giving an AFX zeolite with Si/Al ratio of 11. Similar treatment was employed for the CHA unit cell ($Si_{36}O_{72}$), in which cationic species were placed inside the *cha* cage, giving a Si/Al ratio of 8 after charge-balancing Al substitutions.[36] Fully

relaxed optimizations were performed with fixed lattice parameters (AFX, $a = b = 13.70$ Å, $c = 19.73$ Å, $\alpha = \beta = 90°$, $\gamma = 120°$; CHA, $a = b = 13.68$ Å, $c = 14.77$ Å, $\alpha = \beta = 90°$, $\gamma = 120°$).

3. Results and discussion

3.1 *In situ/operando* spectroscopic studies under steady-state NH_3–SCR conditions

In situ Cu K-edge XANES analysis were carried out under steady-state standard NH_3–SCR conditions (1000 ppm NH_3, 1000 ppm NO, and 10% O_2 with He balance) at varying temperatures (150–400 °C). Three Cu-AFX samples with different Cu loading were used (Table 1). The results for a representative catalyst, Cu4.1-AFX, are shown in Fig. 2a. Catalytic result for NH_3-SCR by Cu4.1-AFX with a laboratory reactor at the same reaction conditions as for *in situ* XANES is shown in Fig. S1. The contact time employed is shorter than that in previous *in situ* XANES studies[44,57,58] for NH_3–SCR by Cu-zeolites, which enables the determination of Cu oxidation states under kinetically controlled conditions below 300 °C where the transfer of the reactants (NO, NH_3, and O_2) to the catalyst particles does not limit the reaction rates, especially at low temperatures. With the rise of temperature, there is an increase in the peak intensity at 8983 eV due to a linear $[Cu(NH_3)_2]^+$ complex.[21,27,44,59] LCF analysis of the XANES spectra was performed using three reference spectra (Fig. 2b): the spectra of solution-phase $[Cu(NH_3)_4]^{2+}$ and $[Cu(NH_3)_2]^+$ at room temperature as well as the spectrum of *in situ* generated Z-Cu^{2+} under a flow of 10% O_2/He at 200 °C. As exemplified in Fig. 2c, the *in situ* XANES spectrum during NH_3–SCR at 200 °C was compared with the best fitting curve using the reference compounds. Fig. 2d-f depicts the temperature dependence of the fractions of different Cu species for the Cu-AFX samples. For all the catalysts, the fraction of Cu(I) species, i.e. $[Cu(NH_3)_2]^+$, is below 50% at low temperature (150 °C) and it increases with the rise of operating temperature (Fig. S2). Assuming the widely accepted redox mechanism of NH_3–SCR, the XANES results indicate that the rate of the SCR reduction half cycle is relatively low at low temperature regime (< 200 °C). In a middle temperature range (200–300 °C), the Cu(II) species (Z-Cu^{2+} and $[Cu(NH_3)_4]^{2+}$) and Cu(I) species ($[Cu(NH_3)_2]^+$) coexist in zeolites, indicating that the rate of the reduction step is comparable to that of the oxidation step. The Cu(II)/Cu(I) ratios for Cu0.4-AFX are lower than those for Cu2.1-AFX and Cu4.1-AFX catalysts in all the temperature regime explored (Fig. S2), which suggests that the rate of oxidation half cycle is relatively slow for the low Cu loading catalyst.[60]

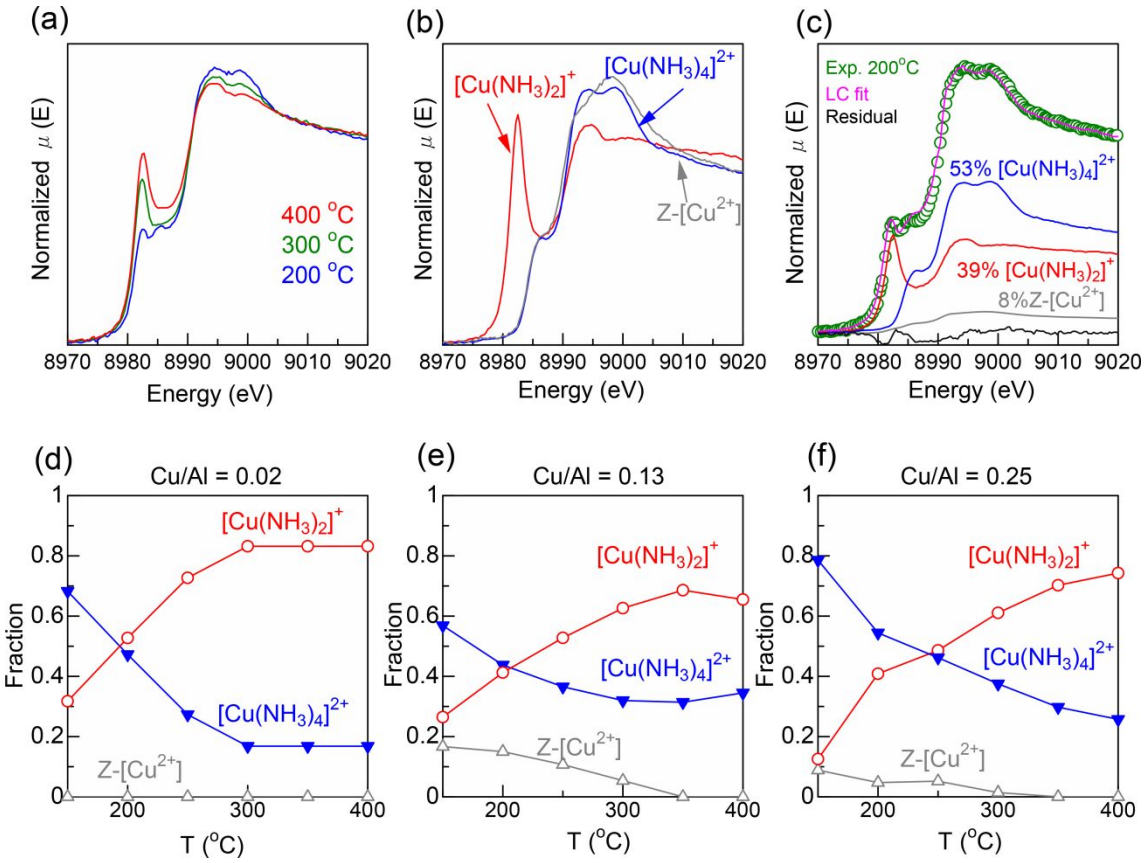

Fig. 2 *In situ* XANES spectra of (a) Cu4.1-AFX under NH_3–SCR conditions with varying temperatures, (b) reference compounds, and (c) LCF analysis at temperature of 200 °C; fraction of Cu species with varying temperatures for (d) Cu0.4-AFX, (e) Cu2.1-AFX, and (f) Cu4.1-AFX catalysts. NH_3–SCR conditions: catalyst weight = 3.8 mg (Cu4.1-AFX), 7.0 mg (Cu2.1-AFX), 38.2 mg (Cu0.4-AFX); 1000 ppm NH_3, 1000 ppm NO, 10% O_2, He balance (1000 mL min^{-1}).

Cu(II) cations in zeolites show a d–d transition band around 730–790 nm.[61–63] Based on the Cu(II)↔Cu(I) redox mechanism, the relative amount of Cu(II) species monitored by diffuse reflectance UV-vis spectroscopy during NH_3–SCR conditions should depend on the concentration of O_2 in the SCR gas mixture. We thus explored the effect of O_2 concentration by *in situ* UV-vis experiments (Fig. 3a), which were performed with Cu4.1-AFX sample at 200 °C under various O_2 concentration (0.1–10%). The spectra exhibit a typical d–d band of Cu(II) species centered around 760 nm. The d-d band intensity (Kubelka-Munk function) at 760 nm was then plotted as a function of the O_2 concentration (Fig. 3b), and simultaneously, N_2 formation in the downstream of the UV-vis cell was monitored by online MS. It should be noted that the MS intensity of N_2 corresponds to the relative rate of NH_3–SCR. The MS intensity of N_2, i.e. the rate of NH_3–SCR, and the relative amount of Cu(II) increase steeply with O_2 concentrations up to 1% O_2, and then level off. In accordance with the redox SCR mechanism, the *in situ* UV-vis experiments indicate that the oxidation rate of Cu(I) is relatively slow under low O_2 pressures (< 1%) but does not limit SCR rate under typical NH_3–SCR conditions (5–10 % O_2) at reaction

temperature of 200 °C for the Cu4.1-AFX sample. This result is consistent with recent reports on the steady-state standard NH_3–SCR process with different O_2 partial pressure over Cu-CHA catalysts.[31,60]

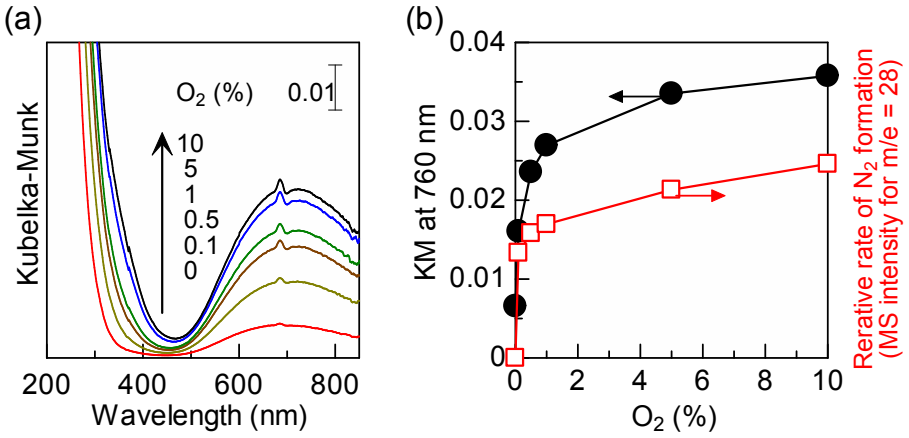

Fig. 3 (a) *In situ* UV-vis spectra of Cu4.1-AFX under transient NH_3–SCR conditions at 200 °C with varying O_2 concentrations; (b) band intensity of Cu(II) under NH_3–SCR conditions and MS intensity of N_2 (m/e = 28) versus O_2 concentrations. NH_3–SCR conditions: sample weight = 10 mg; 500 ppm NH_3, 500 ppm NO, O_2, Ar balance (100 mL min^{-1}).

3.2 Reduction half cycle

To understand the mechanisms of the reduction half cycle, we performed comprehensive *in situ/operando* spectroscopic experiments under transient SCR conditions. First, *operando* IR experiment was carried out for the reaction of preadsorbed NH_3 with NO at reaction temperature of 200 °C. A disc of Cu4.1-AFX in the IR cell was first exposed to a flow of 1000 ppm NH_3/He, followed by He purge. Fig. 4a shows the IR spectrum with a peak at 1620 cm^{-1} assignable to NH_3 adsorbed on the Cu(II) species [Cu(II)-NH_3] and an intense peak of NH_4^+ (NH_3 adsorbed on the BASs) at 1425 cm^{-1}.[64–66] When 500 ppm NO/He was fed to the IR disc, the intensity of the Cu(II)–NH_3 band at1620 cm^{-1} decreased, while the intensity of band due to NH_4^+ at 1450 cm^{-1} increased. Along with the IR measurement, the online MS was used to monitor the N_2 evolution in the outlet gas (Fig. 4b). The N_2 formation was found to coincide with the depletion of NH_3 coordinated to Cu(II) sites (1620 cm^{-1}), which indicates NO reacts with NH_3 on Cu(II) sites to yield N_2 [Cu(II)-NH_3 + NO → Cu(I) + N_2 + H_2O + H^+). This is consistent with DFT investigations on the reduction half cycle of NH_3–SCR.[22,24,27] The concurrent increase of the band intensity at 1450 cm^{-1} in IR spectrum (Fig. 4a) suggests a part of the NH_3 on Cu migrates to the H^+ site to form NH_4^+.

For quantitative discussion of the IR results, we estimated the number of NH_4^+ and Cu(II)-NH_3 using their IR band area and the integrated molar extinction coefficients for NH_4^+ in zeolite (0.03 cm μmol^{-1})[67] and for Cu(II)-NH_3 (0.176 cm μmol^{-1}). The coefficient for Cu(II)-NH_3, NH_3 species adsorbed on Lewis acid sites, was determined by IR/MS experiment of NH_3 adsorption/desorption using a K^+-

exchanged FER zeolite which does not have Brønsted acid sites. As shown in Fig. 4b, the number of NH_3 adsorbed on Cu(II) sites (2.5 mmol g^{-1}) before NO feeding (t = 0 s) was 3.8 times as large as the number of Cu cations in the Cu4.1-AFX sample (0.65 mmol g^{-1}). This value is consistent with the structural model derived from *in situ* XANES analysis; most of the Cu species are present as $[Cu(NH_3)_4]^{2+}$ complexes under NH_3 flow. Additional finding in Fig. 4(a) is that the number of NH_4^+ is increased by the reaction of Cu(II)-NH_3 with NO. Assuming a $[Cu(NH_3)_4]^{2+}$ complex exchanged by two zeolite oxygen sites as an initial state, the reduction half cycle in eqn. (1) is described as

$$[Cu(NH_3)_4]^{2+} + NO \rightarrow [Cu(NH_3)_2]^{+} + H^{+} + N_2 + H_2O$$

The reaction of H^+ with an adsorbed NH_3 could increase the number of NH_4^+. This is consistent with the result by Simon et al. who reported that the number of NH_4^+ increases upon treating the Cu(II)-NH_3 species with NO.[68]

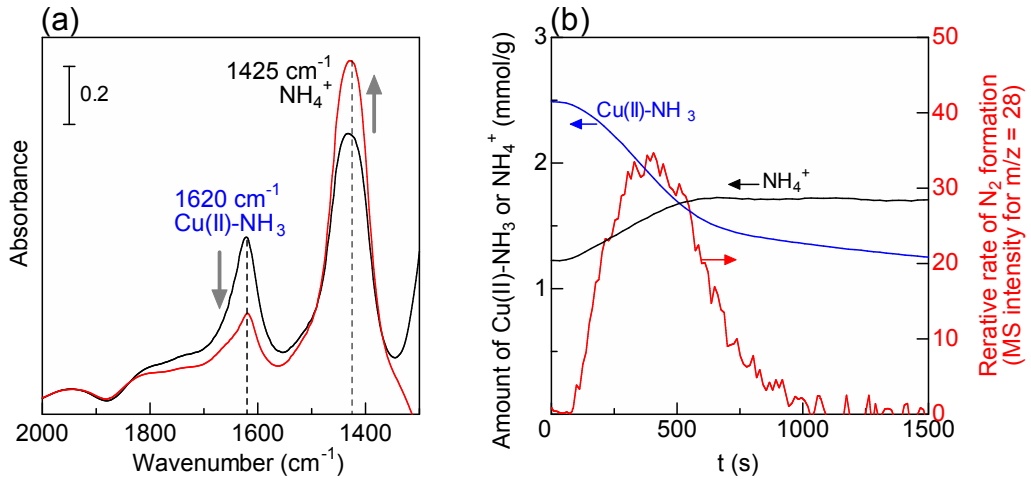

Fig. 4 (a) *Operando* IR spectra of Cu4.1-AFX under transient NH_3–SCR conditions at temperature of 200 °C. The Cu-zeolite sample was first treated by 0.1% NH_3/He flow (100 mL min^{-1}), followed by He purge (black line), and by 500 ppm NO/He flow (100 mL min^{-1}) (red line); (b) Time course of the MS intensity of N_2 (m/e = 28) and the number of NH_4^+ and Cu(II)-NH_3 species estimated by IR peak area. Sample weight = 40 mg.

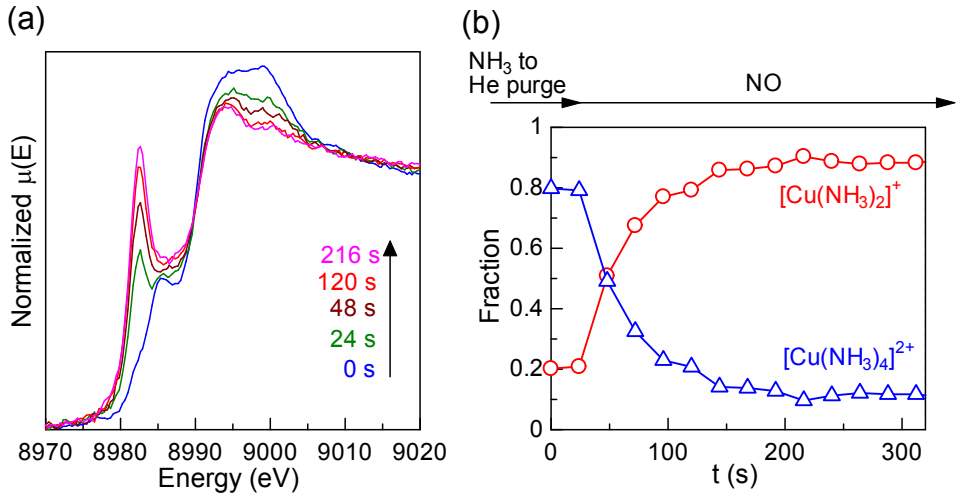

Fig. 5 (a) *In situ* XANES spectra of Cu4.1-AFX under 0.1%NO/He at 200 °C. The sample was pre-exposed to 0.1%NH_3 and He purge; (b) Time course of the fractions of Cu species in Cu4.1-AFX. Sample weight = 3.8 mg; flow rate = 1000 mL min^{-1}.

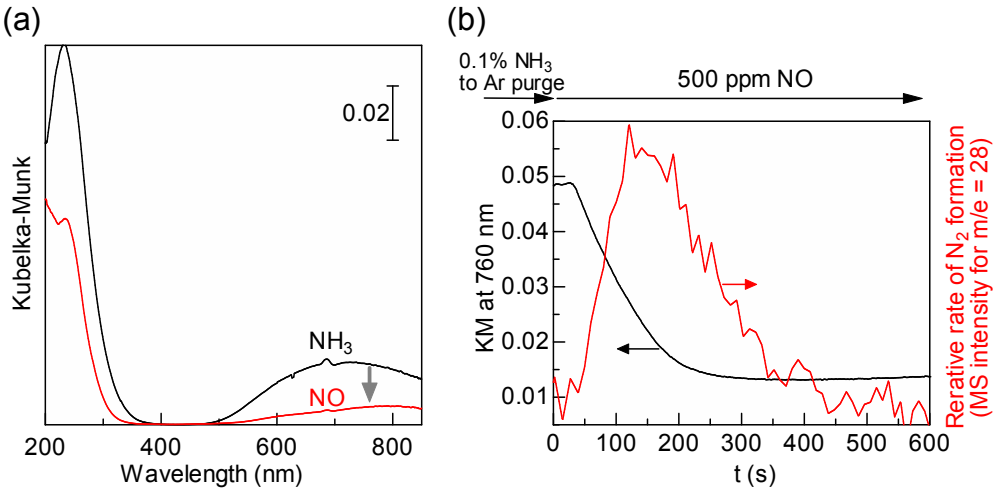

Fig. 6 (a) *Operando* UV-vis spectra of Cu2.1-AFX under transient NH_3–SCR conditions at temperature of 200 °C. The Cu-zeolite sample was first treated by 10% O_2/Ar (100 mL min^{-1}), followed by 0.1% NH_3/Ar flow (100 mL min^{-1}) (black line), and by 500 ppm NO/Ar flow (100 mL min^{-1}) (red line); (b) Time course of the UV-vis band intensity of Cu(II) species and the MS intensity of N_2 (m/e = 28). Sample weight = 10 mg.

In situ XANES experiments were then conducted to monitor the dynamic change of Cu oxidation states at the same transient conditions as the IR experiment. Fig. 5a shows *in situ* XANES spectra of the transient reduction experiments for Cu4.1-AFX at 200 °C. First, 1000 ppm NH_3 was fed to a pre-oxidized catalyst disc, followed by purging with He flow. The XANES spectrum of pre-

oxidized catalyst shows a broad peak at 8998 eV and a shoulder at 8987 eV, which are assigned to isolated Cu(II) ions at negative oxygen sites in zeolites [44]. When NO was fed to the catalyst, a peak at 8983 eV due to the linear $[Cu(NH_3)_2]^+$ complex[21,22] appeared, and its intensity increased with time. LCF analysis with reference spectra of three Cu compounds (Z-$[Cu^{2+}]$, $[Cu(NH_3)_4]^{2+}$, and $[Cu(NH_3)_2]^+$) gave worse fitting result than the analysis with two Cu reference compounds ($[Cu(NH_3)_4]^{2+}$, and $[Cu(NH_3)_2]^+$). Fig. 5b shows the latter LCF data, which describes the fraction of $[Cu(NH_3)_4]^{2+}$ and $[Cu(NH_3)_2]^+$ as a function of NO flowing time. It is clear that $[Cu(NH_3)_4]^{2+}$ species reacts with NO to give $[Cu(NH_3)_2]^+$ species.

Fig. 6 shows the results of *operando* UV-vis measurements for the transient experiment of reduction half cycle at temperature of 200 °C. The UV-vis spectrum of NH_3-preadsorbed Cu2.1-AFX (Fig. 6a) shows the a d-d band of Cu(II) species at 640 nm assignable to Cu(II) complexes with N-containing ligands.[69,70] The result is consistent with the IR result that NH_3 is coordinated to Cu(II) and the XANES result that $[Cu(NH_3)_4]^{2+}$-like species is the major Cu species in the NH_3-preadsorbed catalyst. After purging with Ar flow, the introduction of 500 ppm NO to the Cu(II)–NH_3 complexes in the catalyst results in a decrease in the d–d band intensity. Fig. 6b shows the time course of the d–d band intensity band and the relative rate of N_2 formation (MS intensity for m/e = 28). Clearly, the N_2 formation coincides with consumption of the $[Cu(NH_3)_4]^{2+}$-like species.

Summarizing the results of XANES, IR and UV-vis measurements, it is concluded that the reaction of the $[Cu(NH_3)_4]^{2+}$-like species with NO yields $[Cu(NH_3)_2]^+$ species and H^+ on the catalyst as well as N_2 and H_2O in the gas phase. This conclusion is consistent with the mechanism of the reduction half cycle reported for NH_3–SCR over Cu-CHA where the NH_3 coordinated on the Cu(II) center reacts with NO to produce N_2 and H_2O (via a NH_2NO intermediate) and $Cu(I)(NH_3)_2$.[22] On the other hand, some papers[29,71,72] proposed a different mechanism for the reduction half cycle of NH_3-SCR over Cu-CHA; Cu(II) is reduced by NO to give a HONO intermediate, which reacts with NH_3 to yield the NH_2NO intermediate and H_2O.

$$[NH_3]\text{-}Cu(II)\text{-}OH + NO \rightleftarrows [NH_3]\text{-}Cu(I) + HONO$$

$$[NH_3]\text{-}Cu(I) + HONO \rightarrow Cu(I) + N_2 + 2H_2O$$

However, the following evidences for NH_3-SCR by Cu-zeolites disagree with this mechanism. Previous reports of *in situ* XANES[23] and ESR[30] spectra of Cu-CHA showed that Cu(II) species remain unreduced under NO flow at 200 °C. Our result from *in situ* UV-vis measurements also showed that the band due to Cu(II) ions or Cu(II) nitrate species[73–75] in Cu-AFX remain unchanged when O_2 and NO were consecutively introduced at 150 °C (Fig. S3). These experimental evidences indicate that the reduction of Cu(II) by only NO to give Cu(I) and HONO intermediate does not occur under typical NH_3-SCR conditions using Cu-zeolite catalysts.

3.3 Oxidation half cycle

Similar sets of experiments were conducted to study the oxidation half cycle. Cu-AFX catalysts, pre-reduced by NO + NH_3 mixture, were oxidized by O_2 at 200 °C, and the dynamic changes in the Cu oxidation states were monitored by *in situ* time-resolved XANES and UV-vis. The Cu4.1-AFX sample was first pre-reduced by NO + NH_3 (t = 0 s), and the corresponding *in situ* XANES spectrum shows an intense peak of 1s → 4p transition at 8983 eV, which is characteristic of the $[Cu(NH_3)_2]^+$ species (Fig. 7a). When the zeolite catalyst was exposed to 10% O_2, the intensity of the peak due to $[Cu(NH_3)_2]^+$ at 8983 eV decreased with time. The XANES feature after 500 s, which exhibits a broad peak centered at 8998 eV and a shoulder at 8987 eV, is similar to that of the $[Cu(NH_3)_4]^{2+}$-like species. The time-dependent fractions of Cu species estimated from LCF analysis were then plotted in Fig. 7b, and the result indicates that the $[Cu(NH_3)_2]^+$ species is oxidized by O_2 as the only oxidant. The fraction of the $[Cu(NH_3)_2]^+$ species did not decrease after 300 s, indicating that not all Cu(I) species are oxidized to Cu(II) in the presence of O_2 at long reaction time. The same result was reported by Paolucci et al.[25] for Cu-CHA who explained that two $[Cu(NH_3)_2]^+$ complexes more than 9 Å away to each other cannot be oxidized only by O_2 feed.

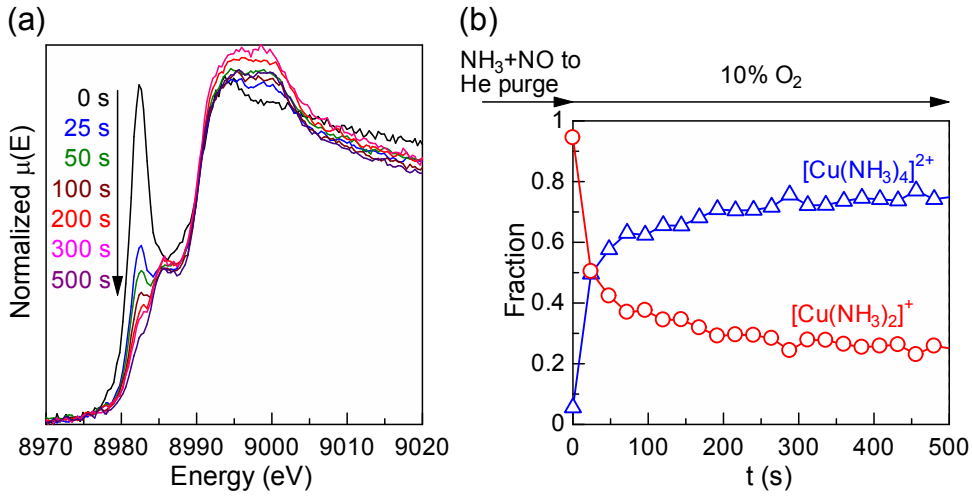

Fig. 7 *In situ* XANES spectra of (a) Cu4.1-AFX under transient reoxidation conditions (10% O_2) at 200 °C. The catalyst sample was pre-reduced by 0.1%NH_3/0.1%NO/He; (b) Time-dependent fractions of Cu species in Cu4.1-AFX. Sample weight = 3.8 mg; flow rate = 1000 mL min^{-1}.

Fig. 8a shows the *in situ* UV-vis spectra of Cu-zeolite samples under transient reoxidation conditions at temperature of 200 °C. After reduction of Cu2.1-AFX by NO + NH_3, the different oxidant mixture of 10% O_2 or 500 ppm NO/10% O_2 was fed to the sample. The d–d transition peak of the Cu(II) species were recovered by these oxidation treatments for 0.5 h, but the intensity of the band did not

markedly depend on the oxidants. This suggests that O_2 rather than NO plays a key role in the oxidation half reaction.

To check the possible oxidation of Cu(I) species by NO or H_2O, we carried out *in situ* UV-vis experiments at 200 °C (Fig. 8b). After reduction by NO+NH_3 mixture, the spectrum of Cu-AFX showed no distinct bands due to Cu(II) species at around 760 nm. When the pre-reduced Cu-AFX was exposed to NO or H_2O, there was almost no increase in the Cu(II) band. The result indicates that NO and H_2O do not oxidize the Cu(I) species at 200 °C. The band observed under NO + O_2 is at higher wavelength than that under O_2, suggesting the differences in the coordination environments of Cu(II) possibly due to adsorption of nitrates on Cu(II).

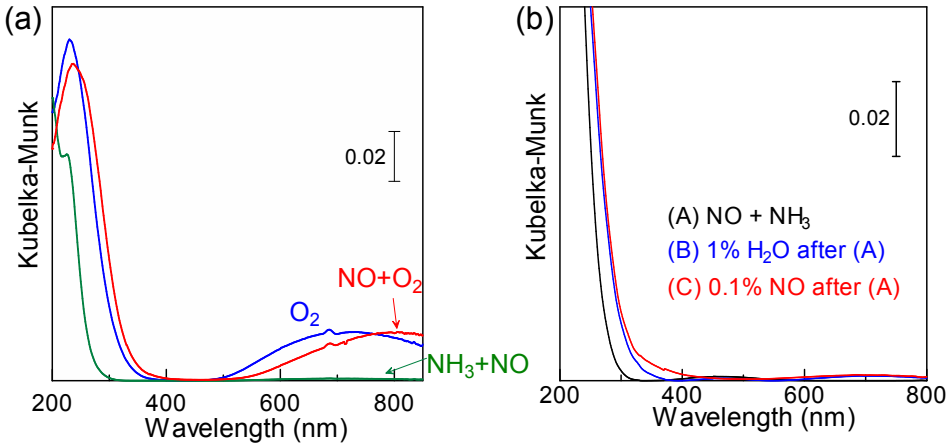

Fig. 8 *In situ* UV-vis spectra of Cu2.1-AFX under transient NH_3–SCR at temperature of 200 °C: (a) The catalyst sample was first reduced by 500 ppm NH_3/ 500 ppm NO/Ar (100 mL min^{-1}) (green line), followed by reoxidation using different oxidants (500 ppm NO+10% O_2 or 10% O_2/Ar); (b) The catalyst sample was first reduced by 500 ppm NH_3/500 ppm NO/1% H_2O/He (100 mL min^{-1}), followed by reoxidation using different oxidants (1% H_2O/He (35 min) or 0.1% NO/He (35 min)).

Prior studies on Cu-CHA suggested the oxidation half cycle occurs via the reaction of O_2 with two $[Cu(NH_3)_2]^+$ to form a dimeric $[Cu_2O_2(NH_3)_4]^{2+}$ [Eqn. (2)], which then releases the mononuclear Cu(II) species with NO assistance [Eqn. (3)]. Our group[31,36] recently found that the oxidation half cycle of the NH_3–SCR on Cu-CHA proceeds by the oxidation of Cu(I) species with O_2 as the sole oxidant and proposed a reaction mechanism of the non-NO-assisted oxidation [Eqn. (4)]. The above presented results from *in situ* spectroscopic measurements over Cu-AFX clearly show the oxidation half cycle also occurs when only O_2 is present as the oxidant. In the following section, we used DFT calculations to explore the O_2-only oxidation mechanism of Cu(I) species over Cu-AFX and compared the key results with Cu-CHA.

3.4 DFT study on oxidation half cycle

3.4.1 Oxidation of Cu(I) by O_2

The oxidation mechanism of Cu(I) species by O_2 as the sole oxidant was proposed on the basis of the stoichiometry [Eqn. (4)], in which four Cu(I) species react with one O_2 molecule to afford four Cu(II) species. The NH_3-solvated $[Cu(NH_3)_2]^+$ ions confined in AFX zeolites were used as starting points to study the oxidation process (Fig. 1). Previous studies on Cu-CHA suggest that the $[Cu(NH_3)_2]^+$ ions in zeolite cages are highly mobile at standard SCR conditions,[22,23,32,44,76] which can diffuse readily across the 8R windows of the neighboring *cha* cages. Considering the structural similarity of AFX and CHA (Fig. 1), we assume that the $[Cu(NH_3)_2]^+$ clusters in AFX behave similar mobility, and their diffusion across different cages will not limit the SCR rate when sufficient amount of Cu is introduced in zeolite (i.e. low Si/Al and high Cu/Al ratios).[24]

Fig. 9 depicts the DFT-optimized structures and the respective energetics of O_2 dissociation over $[Cu(NH_3)_2]^+$ clusters in Cu-AFX. The adsorption of O_2 on a pair of $[Cu(NH_3)_2]^+$ in Cu-AFX is energetically favorable by -37 kJ/mol, in which O_2 interacts with the two Cu centers at a bridging position. The further dissociation of O–O bond proceeds via a two-step mechanism, accompanied with the gradual elongation of O–O distance from 1.28 Å in the adsorption complex to 2.34 Å in the dissociated state. The first step has an activation barrier of 22 kJ/mol and forms the peroxo-dicopper $[Cu_2\text{-peroxo}]^{2+}$, i.e. ($\mu$-$\eta^2$,$\eta^2$-peroxo) dicopper complex. The second step leads to the complete O_2 dissociation to produce $[Cu_2(\mu\text{-}O)_2]^{2+}$, i.e. bis($\mu$-oxo) dicopper complex with an activation barrier of 48 kJ/mol and an endothermicity of 6 kJ/mol. Although our spectroscopic results did not confirm the presence of the Cu-dimer, the predicted higher stability of (μ-η^2, η^2-peroxo) dicopper than bis(μ-oxo) dicopper is consistent with the experimental observations[25,34,35] and the PBE+D+U calculations reported by Chen et al.[37]

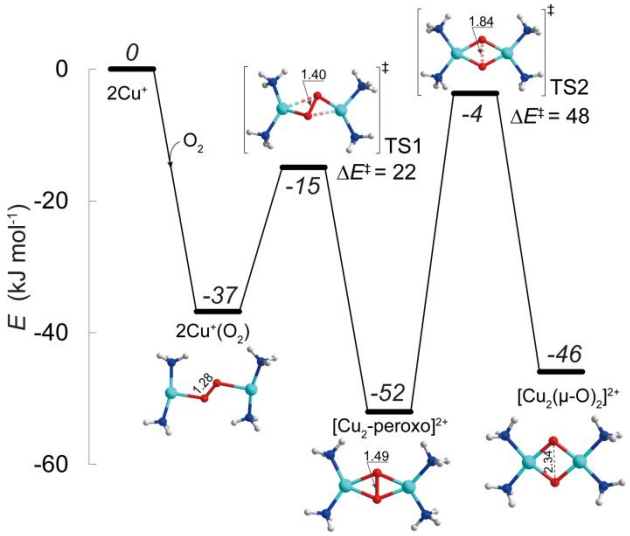

Fig. 9 Reaction energy diagram for the dissociation of O_2 over two $[Cu(NH_3)_2]^+$ clusters in Cu-AFX. The zeolite frameworks are not shown for clarity. The atomic distances are indicated in angstrom (Å).

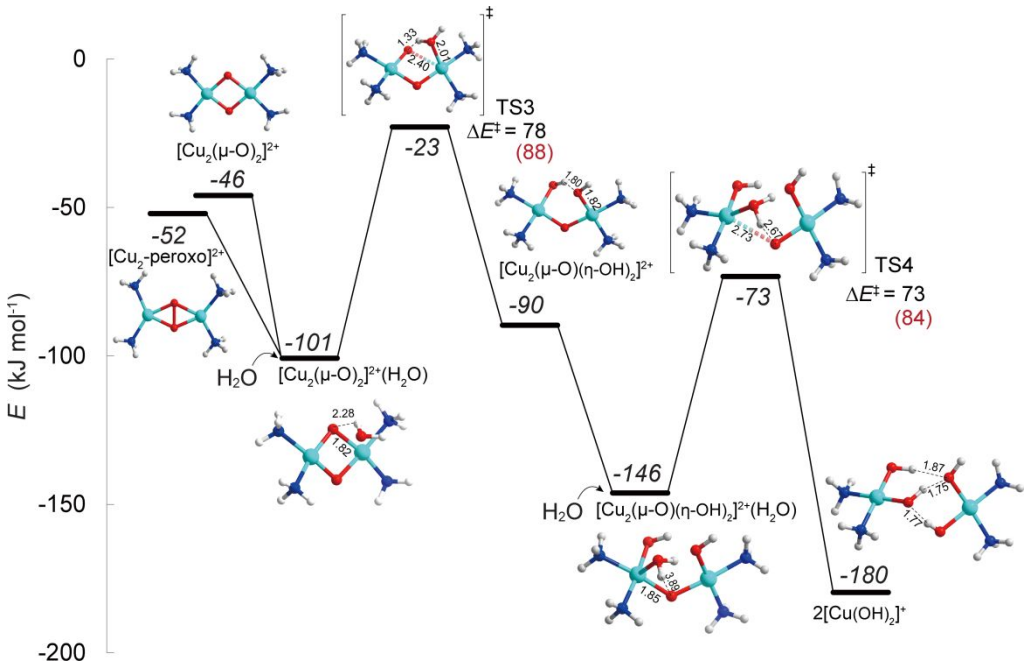

Fig. 10 Reaction energy diagram for H_2O-assisted decomposition of dimeric Cu-oxo complexes to $[Cu(OH)_2]^+$. The respective reaction barriers in Cu-CHA are given in brackets (data were taken from ref. [36]).

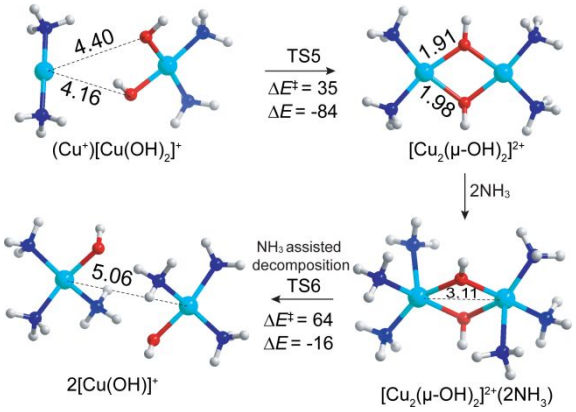

Fig. 11 Production of $[Cu(OH)]^+$ from the reaction of Cu^+ and $[Cu(OH)_2]^+$ ions. $\Delta E^{\ddagger}$ and ΔE (in kJ/mol) are the activation and reaction energies for each elementary step.

In our previous DFT study on Cu-CHA zeolite,[36] we proposed the O_2-only mechanism for the oxidation half cycle of NH_3–SCR, in which the activation of Cu^+ to $[Cu(OH)]^+$ or Cu^{2+} occurs via the sequential hydrolysis reactions of $[Cu_2(\mu\text{-}O)_2]^{2+}$ or $[Cu_4(\mu_3\text{-}O)_2]^{4+}$. The proposed two types of O_2-only activations via the dimeric and tetrameric Cu-oxo clusters show similar reaction barriers and afford the same final stoichiometry as described in Eqn. (4). As experimental studies[24,77] suggested the dimeric Cu-oxo complexes seem more relevant in SCR, herein we only present the dimeric Cu mediated O_2-only mechanism. The water reactant involved in Eqn. (4) can be either from humid reaction atmosphere or the reduction half cycle of SCR (Eqn.(1)). Fig. 10 depicts the reaction energy diagram for the sequential hydrolysis reactions of dimeric Cu-oxo complexes. In the presence of vicinal water, it was found that $[Cu_2\text{-peroxo}]^{2+}$ is first converted to $[Cu_2(\mu\text{-}O)_2]^{2+}$ (Fig. S4) before initializing the dissociation of Cu–O bonds. The adsorption of water molecules over $[Cu_2(\mu\text{-}O)_2]^{2+}$ promotes the dissociation of Cu–O bonds, which produces two mononuclear $[Cu(OH)_2]^+$ intermediates. The activation barriers for the two consecutive hydrolysis reactions are 78 and 73 kJ/mol, respectively. The further conversion of $[Cu(OH)_2]^+$ to desired $[Cu(OH)]^+$ sites occurs by reacting with a Cu^+ site (i.e. $[Cu(NH_3)_2]^+$), which forms a dimeric $[Cu_2(\mu\text{-}OH)_2]^{2+}$ with an activation barrier of 35 kJ/mol (Fig. 11). The next conversion step is assisted by the effect of NH_3 solvation, which produces two $[Cu(OH)]^+$ sites with activation and reaction energies of 64 and -16 kJ/mol. The produced $[Cu(OH)]^+$ species are known to be reactive in the reduction half cycle, which is transformed to Cu(I) species after NH_3/NO reduction.[22] For the O_2-only oxidation mechanism, the reaction steps of Cu-oxo hydrolysis show the highest activation barriers with estimated values of 73–78 kJ/mol. In comparison, the O_2-only oxidation of Cu(I) in Cu-CHA[36] shows similar reaction mechanism but requires higher activation barriers (84–88 kJ/mol, Fig. 10), indicating that a more efficient oxidation half cycle may occur in Cu-AFX than in Cu-CHA. The oxidation barrier difference should be strongly related to the microenvirmoent of the reactive centers, and we speculate the variation in the shape and size of zeolite cage is a key factor for the different reactivity of confined species.

3.4.2 Oxidation of Cu(I) by O_2 + NO

The oxidation of Cu(I) to Cu(II) species with both O_2 and NO was then investigated. We have followed the reaction mechanism proposed for Cu-CHA zeolite, in which NO reacts with the activated dimeric Cu to produce isolated Cu(II) species.[32,36] Either starting from $[Cu_2\text{-peroxo}]^{2+}$or $[Cu_2(\mu\text{-}O)_2]^{2+}$, the presence of a surrounding NO leads to the formation of adsorption structure $[Cu_2(\mu\text{-}O)(ONO)]^{2+}$ as shown in Fig. 12. Then, the oxidation of NO to NO_2 occurs via TS7 with a barrier of 50 kJ/mol to produce adsorbed NO_2 intermediate ($[Cu_2(\mu\text{-}O)(NO_2)]^{2+}$). The further reaction to produce nitrate species $[Cu(NO_3)]^+$ via TS8 requires a barrier of only 25 kJ/mol, which is strongly exothermic by –154 kJ/mol. Therefore, during the NO-assisted oxidation, the production of Cu nitrate species is strongly favorable, and such oxidized Cu(II) nitrates have been also observed in previously reported spectroscopic experiments.[73,78–80] However, the role of such Cu nitrate species remains controversial, and particularly whether they take part in the SCR cycle is not fully confirmed.[81]

To provide insights into the effect of Cu nitrate species on SCR reaction, we further explored their possible conversion reactions (Fig. 13). In the presence of NO, the $[Cu(NO_3)]^+$ is transformed into nitrite species $[Cu(NO_2)]^+$ via a stepwise mechanism (Fig. 13a).[32] First the preabsorbed NO in zeolite pore reacts with $[Cu(NO_3)]^+$, which forms a $[Cu(NO_3NO)]^+$ intermediate. Then NO is oxidized to NO_2 by the NO_3 moiety with a simultaneous production of a $[Cu(NO_2)]^+$. The required barriers are 32 and 73 kJ/mol for the two elementary steps. The produced NO_2-monodentated $[Cu(NO_2)]^+$ can be converted into the NO_2-bidentated form ($[Cu(\eta^2\text{-}NO_2)]^+$) with an activation barrier of 48 kJ/mol (Fig. 13b). To acquire the target production of N_2 and H_2O, it has been proposed that it is necessary to form NH_4NO_2 or NH_2NO intermediates, which can readily decompose to target products.[81] However, the stability evaluation indicates the formation of such intermediates from the Cu nitrite is strongly energetically unfavorable (Fig. 13b). With the reference to the Cu nitrite species, the formation of NH_2NO and NH_4NO_2 is disfavored by 156 and 225 kJ/mol, respectively. Such thermodynamic hindrances may be related to the stable nature of the Cu nitrate/nitrite species,[81] which limits their further conversion to target N_2 and H_2O via unstable NH_2NO or NH_4NO_2 intermediates. Thus, the contribution of the Cu nitrate/nitrite species to the oxidation half cycle of the standard SCR seems less important, and they may only present as off-cycle states, particularly at low temperature ranges. This proposition agrees with the recent experimental studies[78,80] suggesting that the nitrate species are not involved under typical SCR conditions. Based on the above results and discussion, we suggest that the oxidation of Cu(I) species during the SCR reaction is mainly contributed from the oxidation with O_2 as the sole oxidant rather than the NO-assisted oxidation.

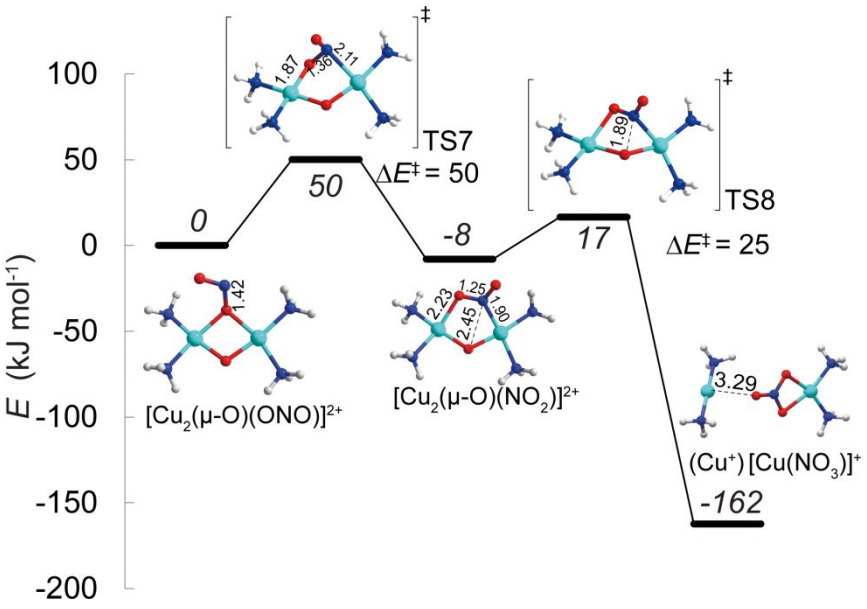

Fig. 12 Reaction energy diagram for the oxidation of Cu(I) via NO assistance in Cu-AFX.

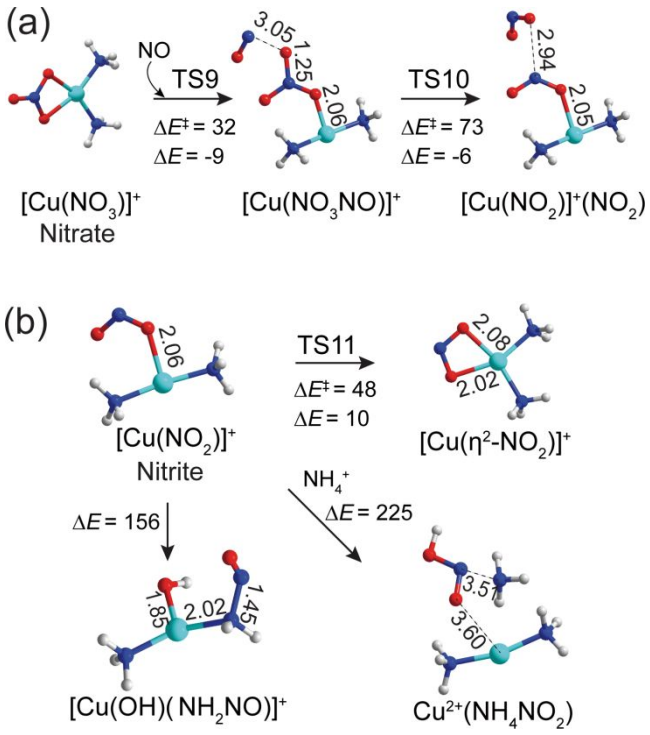

Fig. 13 Conversions of Cu(II) (a) nitrate and (b) nitrite species. $\Delta E^{\ddagger}$ and ΔE (in kJ/mol) are the activation and reaction energies for each elementary step.

4. Conclusions

The NH_3–SCR over Cu-AFX zeolites has been studied using different *in situ/operando* spectroscopic techniques and DFT calculations. Transient reduction experiments using *in situ/operando* XANES, UV-vis, and IR spectroscopies show that, during the reduction half cycle, the NH_3 coordinated on the Cu(II) center rather than NH_4^+ (NH_3 adsorbed on Brønsted acid sites) is reactive with NO to produce N_2 and H_2O, in accompany with the reduction of Cu(II) to Cu(I) species. For the oxidation half cycle, transient *in situ* XANES and UV-vis experiments suggest the Cu(I) species is oxidized with O_2 as the sole oxidant. DFT calculations were further performed to study the oxidation of Cu(I) in Cu-AFX, and the feasible reaction pathways with O_2 as the exclusive oxidant was proposed, in which Cu(I) species react with O_2 to form dimeric Cu-oxo complexes. The decomposition of such Cu-oxo intermediates occurs via hydrolysis reactions, which produces activated isolated Cu(II) species for the consecutive reduction half cycle of NH_3–SCR. The NO-assisted oxidation favors the production of cupric nitrate/nitrite complexes, which show difficulties in further decomposing to target products of N_2 and H_2O as well as the original Cu species to close the catalytic cycle. We posit the oxidation of Cu(I) species with O_2 as the sole oxidant plays the key role in the oxidation half cycle of low-temperature standard NH_3–SCR.[31,34,36]

Conflicts of interest

There are no conflicts to declare.

Acknowledgements

This study is one of the projects promoted by the research association of AICE and financially supported by Japan Ministry of Economy, Trade and Industry and auto industries. This study is also financially supported by the JST-CREST project JPMJCR17J3, KAKENHI grants 17H01341, 20H02518, and 20H02775 from JSPS, and by MEXT projects “Elements Strategy Initiative to Form Core Research Centers” and IRCCS. The authors sincerely acknowledge Prof. Atsushi Satsuma for his help on the UV-vis measurements and the technical division of the Institute for Catalysis (Hokkaido University) for manufacturing experimental equipment. XAS experiments were carried out at the SPring-8 BL-14B2 beamline at JASRI (proposal No. 2019A1614). Part of the calculations were performed on supercomputers at RIIT (Kyushu Univ.) and ACCMS (Kyoto Univ.).

References

1 A. M. Beale, F. Gao, I. Lezcano-Gonzalez, C. H. F. Peden and J. Szanyi, *Chem. Soc. Rev.*, 2015, **44**, 7371–7405.
2 R. Zhang, N. Liu, Z. Lei and B. Chen, *Chem. Rev.*, 2016, **116**, 3658–3721.
3 S. V. Priya, T. Ohnishi, Y. Shimada, Y. Kubota, T. Masuda, Y. Nakasaka, M. Matsukata, K. Itabashi, T. Okubo, T. Sano, N. Tsunoji, T. Yokoi and M. Ogura, *Bull. Chem. Soc. Jpn.*, 2018, **91**, 355–361.
4 M. Mizumoto, N. Yamazoe and T. Seiyama, *J. Catal.*, 1979, **59**, 319–324.
5 T. Komatsu, M. Nunokawa, I. S. Moon, T. Takahara, S. Namba and T. Yashima, *J. Catal.*, 1994, **148**, 427–437.
6 A. Grossale, I. Nova, E. Tronconi, D. Chatterjee and M. Weibel, *Top. Catal.*, 2009, **52**, 1837–1841.
7 A. Wang, Y. Wang, E. D. Walter, N. M. Washton, Y. Guo, G. Lu, C. H. F. Peden and F. Gao, *Catal. Today*, 2019, **320**, 91–99.
8 P. Chen, D. Rauch, P. Weide, S. Schönebaum, T. Simons, M. Muhler, R. Moos and U. Simon, *Catal. Sci. Technol.*, 2016, **6**, 3362–3366.
9 S. Li, Y. Wang, T. Wu and W. F. Schneider, *ACS Catal.*, 2018, **8**, 10119–10130.
10 J. H. Kwak, R. G. Tonkyn, D. H. Kim, J. Szanyi and C. H. F. Peden, *J. Catal.*, 2010, **275**, 187–190.
11 J. S. McEwen, T. Anggara, W. F. Schneider, V. F. Kispersky, J. T. Miller, W. N. Delgass and F. H. Ribeiro, *Catal. Today*, 2012, **184**, 129–144.
12 Y. Xin, Q. Li and Z. Zhang, *ChemCatChem*, 2018, **10**, 29–41.
13 Y. Jangjou, Q. Do, Y. Gu, L. G. Lim, H. Sun, D. Wang, A. Kumar, J. Li, L. C. Grabow and W. S. Epling, *ACS Catal.*, 2018, **8**, 1325–1337.
14 T. Usui, Z. Liu, S. Ibe, J. Zhu, C. Anand, H. Igarashi, N. Onaya, Y. Sasaki, Y. Shiramata, T. Kusamoto and T. Wakihara, *ACS Catal.*, 2018, **8**, 9165–9173.
15 Y. J. Kim, P. S. Kim and C. H. Kim, *Appl. Catal. A Gen.*, 2019, **569**, 175–180.
16 X. Auvray, A. Grant, B. Lundberg and L. Olsson, *Catal. Sci. Technol.*, 2019, **9**, 2152–2162.
17 Y. Shan, X. Shi, G. He, K. Liu, Z. Yan, Y. Yu and H. He, *J. Phys. Chem. C*, 2018, **122**, 25948–25953.
18 D. W. Fickel and R. F. Lobo, *J. Phys. Chem. C*, 2010, **114**, 1633–1640.
19 Z. Liu, T. Wakihara, K. Oshima, D. Nishioka, Y. Hotta, S. P. Elangovan, Y. Yanaba, T. Yoshikawa, W. Chaikittisilp, T. Matsuo, T. Takewaki and T. Okubo, *Angew. Chem. Int. Ed.*, 2015, **54**, 5683–5687.
20 S. H. Krishna, C. B. Jones, J. T. Miller, F. H. Ribeiro and R. Gounder, *J. Phys. Chem. Lett.*, 2020, **11**, 5029–5036.
21 R. Zhang and J. S. McEwen, *J. Phys. Chem. Lett.*, 2018, **9**, 3035–3042.
22 C. Paolucci, A. A. Parekh, I. Khurana, J. R. Di Iorio, H. Li, J. D. Albarracin Caballero, A. J. Shih, T. Anggara, W. N. Delgass, J. T. Miller, F. H. Ribeiro, R. Gounder and W. F. Schneider, *J. Am. Chem. Soc.*, 2016, **138**, 6028–48.
23 T. V. W. Janssens, H. Falsig, L. F. Lundegaard, P. N. R. Vennestrøm, S. B. Rasmussen, P. G. Moses, F. Giordanino, E. Borfecchia, K. A. Lomachenko, C. Lamberti, S. Bordiga, A. Godiksen, S. Mossin and P. Beato, *ACS Catal.*, 2015, **5**, 2832–2845.
24 F. Gao, D. Mei, Y. Wang, J. Szanyi and C. H. F. Peden, *J. Am. Chem. Soc.*, 2017, **139**, 4935–4942.
25 C. Paolucci, I. Khurana, A. A. Parekh, S. Li, A. J. Shih, H. Li, J. R. Di Iorio, J. D. Albarracin-Caballero, A. Yezerets, J. T. Miller, W. N. Delgass, F. H. Ribeiro, W. F. Schneider and R. Gounder, *Science*, 2017, **357**, 898–903.
26 G. E. Douberly, A. M. Ricks, P. V. R. Schleyer and M. A. Duncan, *J. Phys. Chem. A*, 2008, **112**, 4869–4874.
27 C. Paolucci, A. A. Verma, S. A. Bates, V. F. Kispersky, J. T. Miller, R. Gounder, W. N. Delgass, F. H. Ribeiro and W. F. Schneider, *Angew. Chem. Int. Ed.*, 2014, **53**, 11828–11833.
28 Y. Li, J. Deng, W. Song, J. Liu, Z. Zhao, M. Gao, Y. Wei and L. Zhao, *J. Phys. Chem. C*, 2016, **120**, 14669–14680.
29 L. Chen, T. V. W. Janssens, P. N. R. Vennestrøm, J. Jansson, M. Skoglundh and H. Grönbeck, *ACS Catal.*, 2020, **10**, 5646–5656.

30 A. Godiksen, O. L. Isaksen, S. B. Rasmussen, P. N. R. Vennestrøm and S. Mossin, *ChemCatChem*, 2018, **10**, 366–370.
31 C. Liu, H. Kubota, T. Amada, K. Kon, T. Toyao, Z. Maeno, K. Ueda, J. Ohyama, A. Satsuma, T. Tanigawa, N. Tsunoji, T. Sano and K. Shimizu, *ChemCatChem*, 2020, **12**, 3050–3059.
32 L. Chen, H. Falsig, T. V. W. Janssens and H. Grönbeck, *J. Catal.*, 2018, **358**, 179–186.
33 H. Falsig, P. N. R. Vennestrøm, P. G. Moses and T. V. W. Janssens, *Top. Catal.*, 2016, **59**, 861–865.
34 C. Negri, T. Selleri, E. Borfecchia, A. Martini, K. A. Lomachenko, T. V. W. Janssens, M. Cutini, S. Bordiga and G. Berlier, *J. Am. Chem. Soc.*, 2020, **142**, 15884–15896.
35 A. Oda, H. Shionoya, Y. Hotta, T. Takewaki, K. Sawabe and A. Satsuma, *ACS Catal.*, 2020, **10**, 12333–12339.
36 C. Liu, H. Kubota, T. Toyao, Z. Maeno and K. Shimizu, *Catal. Sci. Technol.*, 2020, **10**, 3586–3593.
37 L. Chen, T. V. W. Janssens and H. Grönbeck, *Phys. Chem. Chem. Phys.*, 2019, **21**, 10923–10930.
38 N. Nakazawa, S. Inagaki and Y. Kubota, *Adv. Porous Mater.*, 2016, **4**, 219–229.
39 D. W. Fickel, E. D'Addio, J. A. Lauterbach and R. F. Lobo, *Appl. Catal. B Environ.*, 2011, **102**, 441–448.
40 N. Martín, C. Paris, P. N. R. Vennestrøm, J. R. Thøgersen, M. Moliner and A. Corma, *Appl. Catal. B Environ.*., 2017, **217**, 125–136.
41 G. Shibata, W. Eijima, R. Koiwai, K. Shimizu, Y. Nakasaka, Y. Kobashi, Y. Kubota, M. Ogura and J. Kusaka, *Catal. Today*, 2019, **332**, 59–63.
42 A. Chokkalingam, W. Chaikittisilp, K. Iyoki, S. H. Keoh, Y. Yanaba, T. Yoshikawa, T. Kusamoto, T. Okubo and T. Wakihara, *RSC Adv.*, 2019, **9**, 16790–16796.
43 B. Ravel and M. Newville, *J. Synchrotron Radiat.*, 2005, **12**, 537–541.
44 K. A. Lomachenko, E. Borfecchia, C. Negri, G. Berlier, C. Lamberti, P. Beato, H. Falsig and S. Bordiga, *J. Am. Chem. Soc.*, 2016, **138**, 12025–12028.
45 G. Kresse and J. Hafner, *Phys. Rev. B*, 1993, **48**, 13115–13118.
46 G. Kresse and J. Hafner, *Phys. Rev. B*, 1994, **49**, 14251–14269.
47 G. Kresse and J. Furthmüller, *Phys. Rev. B*, 1996, **54**, 11169–11186.
48 J. P. Perdew, K. Burke and M. Ernzerhof, *Phys. Rev. Lett.*, 1996, **77**, 3865–3868.
49 P. E. Blöchl, *Phys. Rev. B*, 1994, **50**, 17953–17979.
50 D. Joubert, *Phys. Rev. B*, 1999, **59**, 1758–1775.
51 J. D. Pack and H. J. Monkhorst, *Phys. Rev. B*, 1977, **16**, 1748–1749.
52 S. Grimme, S. Ehrlich and L. Goerigk, *J. Comput. Chem.*, 2011, **32**, 1456–1465.
53 G. Henkelman and H. Jónsson, *J. Chem. Phys.*, 2000, **113**, 9978–9985.
54 L. Y. Isseroff and E. A. Carter, *Phys. Rev. B*, 2012, **85**, 235142.
55 C. Baerlocher and L. B. McCusker, Database of Zeolite Structures: http://www.iza-structure.org/databases/.
56 C. Liu, I. Tranca, R. A. Van Santen, E. J. M. Hensen and E. A. Pidko, *J. Phys. Chem. C*, 2017, **121**, 23520–23530.
57 K. Ueda, J. Ohyama and A. Satsuma, *Chem. Lett.*, 2017, **46**, 1390–1392.
58 A. G. Greenaway, I. Lezcano-Gonzalez, M. Agote-Aran, E. K. Gibson, Y. Odarchenko and A. M. Beale, *Top. Catal.*, 2018, **61**, 175–182.
59 B. Kerkeni, D. Berthout, D. Berthomieu, D. E. Doronkin, M. Casapu, J. Grunwaldt and C. Chizallet, *J. Phys. Chem. C*, 2018, **122**, 16741–16755.
60 C. B. Jones, I. Khurana, S. H. Krishna, A. J. Shih, W. N. Delgass, J. T. Miller, F. H. Ribeiro, W. F. Schneider and R. Gounder, *J. Catal.*, 2020, **389**, 140–149.
61 A. Godiksen, F. N. Stappen, P. N. R. Vennestrøm, F. Giordanino, S. B. Rasmussen, L. F. Lundegaard and S. Mossin, *J. Phys. Chem. C*, 2014, **118**, 23126–23138.
62 R. Oord, I. C. Ten Have, J. M. Arends, F. C. Hendriks, J. Schmidt, I. Lezcano-Gonzalez and B. M. Weckhuysen, *Catal. Sci. Technol.*, 2017, **7**, 3851–3862.
63 F. Giordanino, P. N. R. Vennestrøm, L. F. Lundegaard, F. N. Stappen, S. Mossin, P. Beato, S. Bordiga and C. Lamberti, *Dalt. Trans.*, 2013, **42**, 12741–12761.
64 H. Zhu, J. H. Kwak, C. H. F. Peden and J. Szanyi, *Catal. Today*, 2013, **205**, 16–23.

65 I. Lezcano-Gonzalez, U. Deka, B. Arstad, A. Van Yperen-De Deyne, K. Hemelsoet, M. Waroquier, V. Van Speybroeck, B. M. Weckhuysen and A. M. Beale, *Phys. Chem. Chem. Phys.*, 2014, **16**, 1639–1650.

66 Y. Shan, X. Shi, J. Du, Y. Yu and H. He, *Catal. Sci. Technol.*, 2019, **9**, 106–115.

67 S. Sultana, S. M. A. H. Siddiki, A. S. Touchy, S. Yasumura, T. Toyao, Z. Maeno and K. Shimizu, *J. Catal.*, 2018, **368**, 145–154.

68 P. Chen, V. Rizzotto, K. Xie and U. Simon, *React. Chem. Eng.*, 2019, **4**, 986–994.

69 K. Shimizu, H. Maeshima, H. Yoshida, A. Satsuma and T. Hattori, *Phys. Chem. Chem. Phys.*, 2001, **3**, 862–866.

70 E. Borfecchia, C. Negri, K. A. Lomachenko, C. Lamberti, T. V. W. Janssens and G. Berlier, *React. Chem. Eng.*, 2019, **4**, 1067–1080.

71 J. H. Kwak, J. H. Lee, S. D. Burton, A. S. Lipton, C. H. F. Peden and J. Szanyi, *Angew. Chem. Int. Ed.*, 2013, **52**, 9985–9989.

72 N. Usberti, F. Gramigni, N. D. Nasello, U. Iacobone, T. Selleri, W. Hu, S. Liu, X. Gao, I. Nova and E. Tronconi, *Appl. Catal. B Environ.*, 2020, **279**, 119397.

73 C. Negri, E. Borfecchia, M. Cutini, K. A. Lomachenko, T. V. W. Janssens, G. Berlier and S. Bordiga, *ChemCatChem*, 2019, **11**, 3828–3838.

74 C. Negri, M. Signorile, N. G. Porcaro, E. Borfecchia, G. Berlier, T. V. W. Janssens and S. Bordiga, *Appl. Catal. A Gen.*, 2019, **578**, 1–9.

75 C. Tyrsted, E. Borfecchia, G. Berlier, K. A. Lomachenko, C. Lamberti, S. Bordiga, P. N. R. Vennestrøm, T. V. W. Janssens, H. Falsig, P. Beato and A. Puig-Molina, *Catal. Sci. Technol.*, 2016, **6**, 8314–8324.

76 F. Giordanino, E. Borfecchia, K. A. Lomachenko, A. Lazzarini, G. Agostini, E. Gallo, A. V. Soldatov, P. Beato, S. Bordiga and C. Lamberti, *J. Phys. Chem. Lett.*, 2014, **5**, 1552–1559.

77 C. Paolucci, J. R. Di Iorio, W. F. Schneider and R. Gounder, *Acc. Chem. Res.*, 2020, **53**, 1881–1892.

78 Y. Zhang, Y. Peng, K. Li, S. Liu, J. Chen, J. Li, F. Gao and C. H. F. Peden, *ACS Catal.*, 2019, **9**, 6137–6145.

79 A. G. Greenaway, A. Marberger, A. Thetford, I. Lezcano-González, M. Agote-Arán, M. Nachtegaal, D. Ferri, O. Kröcher, C. R. A. Catlow and A. M. Beale, *Chem. Sci.*, 2020, **11**, 447–455.

80 A. Marberger, A. W. Petrov, P. Steiger, M. Elsener, O. Kröcher, M. Nachtegaal and D. Ferri, *Nat. Catal.*, 2018, **1**, 221–227.

81 F. Gao and C. H. F. Peden, *Catalysts*, 2018, **8**, 140.